Revealing the Crystalline Packing Structure of Y6 in the Active Layer of Organic Solar Cells: The Critical Role of Solvent Additives

Xinxin Xia, Le Mei, Chengliang He, Zeng Chen, Nannan Yao, Minchao Qin, Rui Sun, Zhenzhen Zhang, Yuyu Pan, Yiqun Xiao, Yuze Lin, Jie Min, Fengling Zhang, Haiming Zhu, Jean-Luc Bredas, Hongzheng Chen, Xian-Kai Chen*, and Xinhui Lu**

X. Xia, M. Qin, Y. Xiao, and Prof. X. Lu
Department of Physics, The Chinese University of Hong Kong, New Territories, Hong Kong
E-mail: xinhui.lu@cuhk.edu.hk

L. Mei, Y. Pan, and Prof. X.-K. Chen
Department of Chemistry, Department of Materials Science and Engineering, City University of Hong Kong, Kowloon, Hong Kong
Hong Kong Institute for Advanced Study, City University of Hong Kong, Hong Kong
E-mail: xche22@cityu.edu.hk

C. He and Prof. H. Chen
State Key Laboratory of Silicon Materials, MOE Key Laboratory of Macromolecular Synthesis and Functionalization, Department of Polymer Science and Engineering, Zhejiang University, Hangzhou, P. R. China
E-mail: hzchen@zju.edu.cn

Z. Chen and Prof. H. Zhu
Center for Chemistry of High-Performance & Novel Materials, Department of Chemistry, Zhejiang University, Hangzhou 310027, Zhejiang, China

N. Yao and Prof. F. Zhang
Department of Physics, Chemistry and Biology (IFM), Linköping University, Linköping, SE-58183, Sweden

R. Sun and Prof. J. Min
The Institute for Advanced Studies, Wuhan University, Wuhan 430072, China

Prof. J.-L. Bredas
Department of Chemistry and Biochemistry, The University of Arizona, Tucson, Arizona 85721-0088, USA

Z. Zhang and Prof. Y. Lin
Beijing National Laboratory for Molecular Sciences, CAS Key Laboratory of Organic Solids, Institute of Chemistry, Chinese Academy of Sciences, Beijing 100190, China

X. Xia and L. Mei contribute equally to this work.

Abstract

The bulk heterojunction (BHJ) morphology of photovoltaic materials is crucial to the fundamental optoelectronic properties of organic solar cells (OSCs). However, in the photoactive layer, the intrinsic crystalline packing structure of Y6, currently the hallmark molecule among the Y-series non-fullerene acceptors (NFAs), has not been unambiguously determined. Here, employing grazing-incidence wide-angle x-ray scattering (GIWAXS), we managed to uncover the intrinsic crystalline packing structure of Y6 in BHJ active layer of OSC, which is found different from its single-crystal structure reported previously. Moreover, we find that solvent additive 1-chloronaphthalene (CN) can induce highly ordered packing of Y6 in BHJ thin films. With the help of atomistic molecular dynamics simulations, it is revealed that π-π interactions generally exist between naphthalene derivatives and IC terminals of Y6 analogues, which would essentially improve their long-range ordering. Our work reveals the intrinsic crystalline packing structure of Y6 in BHJ active layer as well as its crystallization mechanism in thin film, thus providing direct correlations between this crystalline packing and the device characteristics and photophysical properties.

Keywords: crystalline packing structure, Y6, device active layer, GIWAXS, solvent additives, molecular dynamics simulations

1. Introduction

The field of organic photovoltaics (OPV) has recently attracted tremendous efforts on the development of novel non-fullerene acceptor (NFA) materials[1-12]. The record power conversion efficiency (PCE) has progressively increased to over 19% since the development of the two most important NFA molecules - ITIC in 2015[12] and Y6 in 2019[6]. The NFA molecules usually possess relatively rigid and planar backbones. This feature facilitates intermolecular π-π stacking to form pure crystalline domains embedded in the amorphous donor/acceptor intermixed regions, giving rise to a so-called "semi-crystalline" active layer. The crystalline packing structure of NFA molecules in the active layer has been shown to play a critical role in the fundamental optoelectronic properties relevant to OPV, e.g., electronic structure, optical absorption, exciton diffusion, polaron generation, and charge transfer, transport, and recombination, which ultimately impact the overall OPV device performance[13-22]. However, the characterization of the crystalline packing structures of recently developed NFA molecules in BHJ active layer and understanding on their underlying formation mechanism still lag far behind the development of OPV materials.

In particular, the Y-series molecules[4-8,23-26], which typically display a banana-shaped backbone in sharp contrast with the essentially linear backbone of ITIC and its derivatives[12,27-29], are expected to have crystalline packing structures distinct from that of ITIC. Single-crystal X-ray diffraction (XRD) is known as an important method to investigate the crystalline structure of organic small molecules. Generally, detailed crystal lattice parameters and monomolecular configurations within the unit cell can be favorably resolved with high

accuracy from XRD data of the corresponding single crystals[19, 30-32]. For example, previous literatures reported a three-dimensional (3D) polymer-like crystalline packing structure in Y6 single crystals[20,32]. Nevertheless, not all NFA molecules can be used to grow single crystals due to the complexity of intermolecular interactions. Moreover, considering the growth process of the single crystals, especially the diverse solvents used and the absence of additives that can possibly affect the crystallization process of NFAs during film casting, it is convenient to realize that the formation thermodynamics and kinetics of single crystals should be to some extent different from that of the crystallites in BHJ active layer fabricated by spin coating[33]. Therefore, it is not straightforward enough to directly transfer the crystal lattices in Y6 single crystals to BHJ films. Grazing-incidence Wide-Angle X-ray Scattering (GIWAXS) has been recognized as an effective technique to characterize the molecular-level 3D crystalline morphology of thin films [34-37]. However, in BHJ active layer of organic solar cells (OSCs), due to the semi-crystalline nature of NFAs and the overlapping with scattering signals from donor polymer, it is usually challenging to probe the relatively complete crystalline features of Y6 directly from its BHJ blend film via GIWAXS[35]. Previously, Xiao et al. identified a 2D square lattice of Y6 with backbone-on orientation from GIWAXS[36], whereas a thermal annealing treatment under 250 °C was required for the thin films to obtain the clear scattering patterns, making it not convincing enough to represent the crystalline structure of Y6 in BHJ thin films prepared under regular device conditions. Therefore, the clear physical picture for crystalline structure of Y6 and its derivatives in BHJ active layer is still to be studied.

Although the crystal-structure of Y6 in the active layer has not been unambiguously

determined, several film-treatment methods have been developed and employed to control the crystallinity and BHJ morphology of the films, thus regulating device performances, among which additive-engineering is one of the frequently used strategies[38-41]. For instance, Huang et al. reported that their newly synthesized solid additive SAD2, which has a planar conformation, can promote the crystallinity of Y6[38]. Such crystallinity improvement was often assumed to be originated from the sublimation of the solid additive upon thermal treatment, which leaves open space for the self-assembly of acceptor molecules[41]. However, in this case, the scattering peak intensity merely increased but did not produce more Bragg peaks for a clear diffraction pattern indexing. Besides, previous studies on the morphological influence of additives also suggested that solvent additives with high boiling points could change the drying speed of the precursor solution and consequently the film formation kinetics or modify the respective solubilities of the donor (D) and acceptor (A) components and thus affect the D/A miscibility[39]. However, the underlying mechanism of how an additive affects or fine tunes the crystalline packing of Y6 is not yet fully understood, and selecting additives to optimize the morphology of its BHJ system is usually an empirical and trial-and-error process.

In the present work, well-defined Bragg peaks of crystalline Y6 are observed in the GIWAXS pattern of a pure Y6 film with 0.5vol% 1-chloronaphthalene (CN) additive, even without the help of thermal annealing. Also, Y6 clearly inherits the same packing motif in the PM6:Y6 blend film fabricated under optimized device conditions (0.5vol% CN and annealing at 80 °C). *As a result*, *the intrinsic crystalline packing structure of Y6 in the device active layer is successfully revealed*, which is found evidently different from its previous single-crystal

structure. These findings therefore provide a new understanding on crystalline packing of Y6 in BHJ of real OSC devices and help uncover the direct correlation between the crystalline structure of Y6 and its device characteristics, e.g., hole transfer dynamics and voltage loss. Furthermore, molecular dynamics (MD) simulations were performed to elucidate the critical role of CN in promoting the crystalline packing of Y6. The simulation data find that it is the π-π interactions between the CN molecules and the IC-2F end groups of Y6 that can act as a bridge for Y6 molecules to connect and stack with each other to form long-range ordering in thin films. Moreover, we find that such π-π interactions generally exist between naphthalene derivatives and IC terminals of symmetric Y-series NFAs, thus implying a promising pathway to optimize the performance of OSCs through fine tuning the crystalline morphology of NFAs.

2. Results and Discussion

2.1 Crystalline packing structure of Y6 in thin films

The molecular structure of Y6 is shown in **Figure 1a**; it features a banana-shaped A-D-A'-D-A backbone configuration with alternating electron deficient (A, A') and rich (D) moieties. For the prototypical PM6:Y6 system, addition of 0.5vol% CN (**Figure 1a**) and thermal annealing at 80 °C are common device fabrication conditions capable of delivering decent PCEs of ~16%[6]. To explore the crystalline packing of Y6 in active layer, we first measured the GIWAXS patterns of a pure Y6 film prepared with 0.5vol% CN. Intriguingly, as shown in **Figure 1b**, the GIWAXS pattern displays discrete and sharp Bragg peaks at (q_r, q_z) = (0.22, 0), (0.44, 0), (0.22, 0.48), (0.22, 0.62), (0.28, 0.18) and (0.46, 0.31) $Å^{-1}$, as well as the π-π peak at

(q_r, q_z) = (0, 1.79) $Å^{-1}$, pointing to the formation of long-range ordered crystalline domains of Y6. On the other hand, thermal annealing at the optimized temperature of 80 °C does not induce any notable changes in the crystalline packing motif of Y6, as evidenced from the nearly identical GIWAXS patterns with or without thermal annealing (**Figure S1-2**).

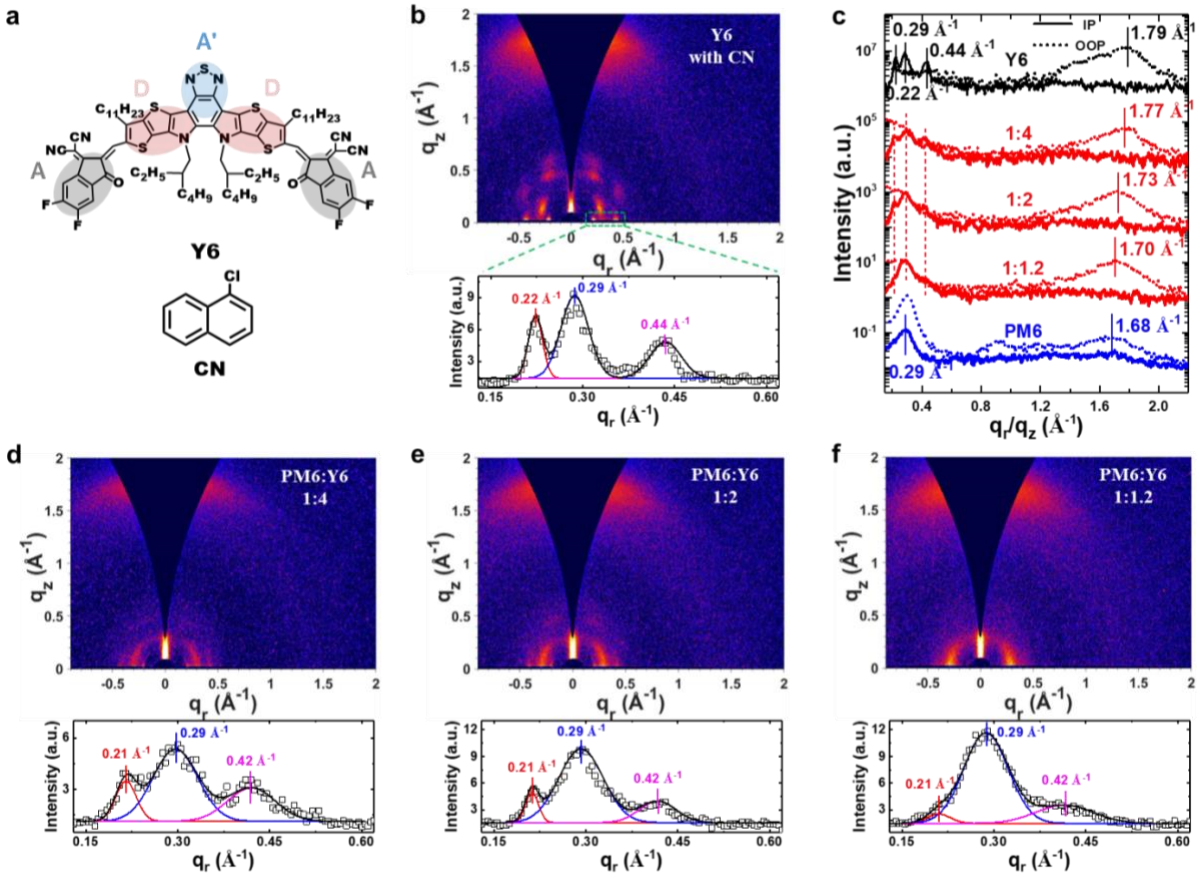

Figure 1. GIWAXS measurements of Y6 pure and blend films. (a) Molecular structure of Y6 and CN. **(b)** GIWAXS 2D pattern and q_r peak fittings in the small q region of Y6 pure film. **(c)** GIWAXS 1D linecuts along in-plane (IP) and out-of-plane (OOP) directions for PM6, Y6 and PM6:Y6 blend films with various D/A ratios. 2D GIWAXS patterns and q_r peak fittings in the small q region of PM6:Y6 blend films with D/A ratio of **(d)** 1:4, **(e)** 1:2 and **(f)** 1:1.2. All the films are prepared with 0.5vol% CN and thermal annealing at 80 °C for 10 mins.

To confirm that the observed crystalline packing structure of Y6 is also present in the actual device active layer, we measured the GIWAXS patterns of PM6:Y6 blend films with 0.5vol% CN and 80 °C annealing. Note here that, in this study, chloroform (CF) is used as the

solvent for solution processing of all thin films, consistent with the reported fabrication condition of the high efficiency PM6:Y6 device active layer[6]. To consider the dilution effect of PM6 in the blend film, we gradually increased the mass ratio of PM6 towards the optimized D/A ratio of 1:1.2. The 2D GIWAXS patterns and the corresponding intensity profiles are presented in **Figure 1c-f**. At the D/A ratio of 1:4, the scattering peaks from the π-π and lamellar stackings of PM6 present at q_z = 1.68 Å^{-1} and q_r = 0.29 Å^{-1}, respectively (**Figure 1c-d** and **Figure S3**), which are expected to largely overlap with the scattering signals from Y6. Remarkably, however, the two feature scattering peaks of crystalline Y6 along q_r can still be identified at q_r = 0.21 and 0.42 Å^{-1}, implying that the incorporation of PM6 does not significantly alter but slightly loosens the crystalline packing of Y6. When the PM6 concentration increases, stronger PM6 signals are observed, while Y6 signals are further weakened but can still be identified at the same positions, as indicated by the triple-peak fitting of intensity profiles in the small q_r region in **Figure 1d-f**. Therefore, we infer that the crystalline packing motif observed in the pure Y6 film remains in the PM6:Y6 blend films fabricated under actual device conditions, although PM6 could override the CN effect and leads to the largely suppressed Y6 crystallization. To further demonstrate that CN plays here a critical role in the crystalline packing of Y6, GIWAXS patterns were measured for PM6:Y6 blend films with a fixed D/A ratio of 1:1.2 and a varying CN content. As shown in **Figure S4**, it is clear that when the CN content gradually increases to 2vol%, the two feature scattering peaks of crystalline Y6 at (q_r, q_z) = (0.22, 0) Å^{-1} and (0.44, 0) Å^{-1} can be clearly identified in the scattering pattern of the blend film, indicating the direct impact of CN in the formation of Y6 crystallites in the BHJ film.

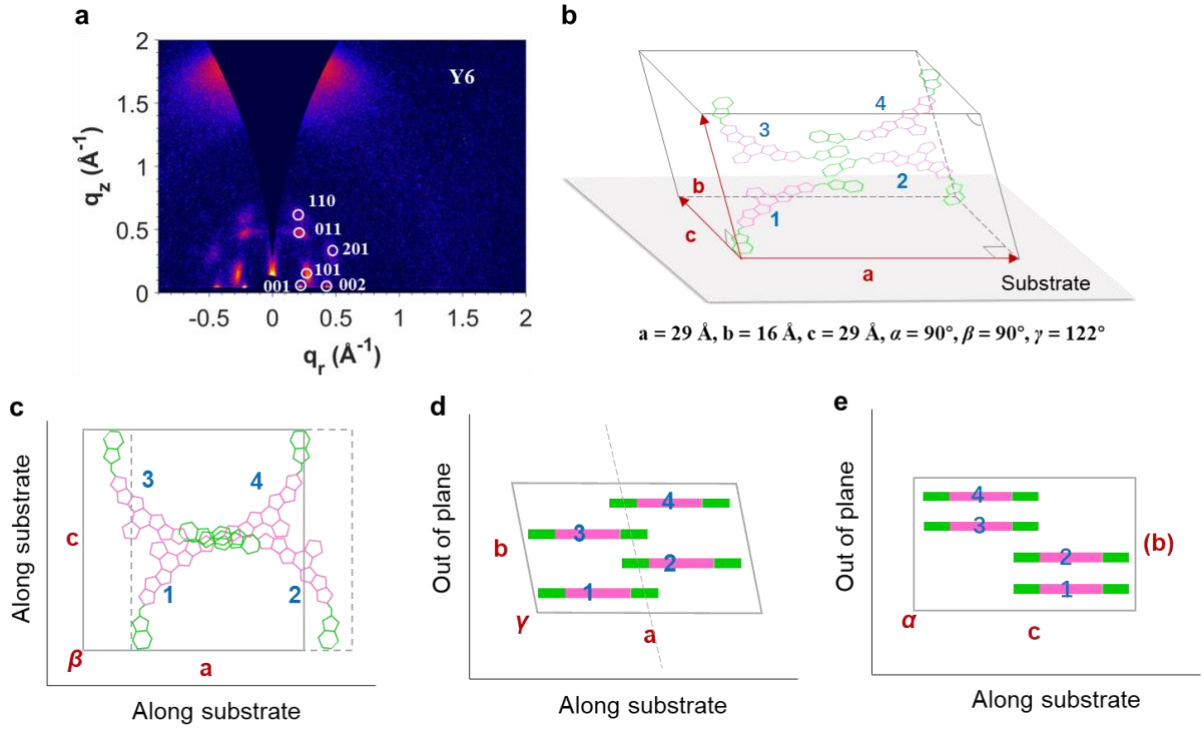

Figure 2. Crystal structure of Y6 in thin film. (a) GIWAXS pattern indexing for Y6 neat film with CN additive and no annealing. **(b)** Illustration of the crystal unit cell of Y6 in real space and the corresponding **(c)** top view, **(d)** front view and **(e)** side view of the unit cell.

To elucidate the crystalline packing structure of Y6 in the active layer, the GIWAXS pattern of the pure Y6 film with 0.5vol% CN was indexed in detail. As shown in **Figure 2a**, the scattering peaks (q_r, q_z) = (0.22, 0), (0.44, 0), (0.22, 0.48), (0.22, 0.62), (0.28, 0.18) and (0.46, 0.31) Å^{-1} can be indexed with a monoclinic unit cell and lattice parameters **a** = 29 Å^{-1}, **b** = 16 Å^{-1}, **c** = 29 Å^{-1}, α = 90°, β = 90° and γ = 122° (**Figure 2b**). The square **ac** plane lies in the in-plane (IP) direction and the rectangular **bc** plane is 32° inclined with respect to the out-of-plane (OOP) direction. The corresponding Miller indices are labeled next to each peak. After resolving the unit-cell structure, we considered in detail the molecular arrangements within the individual unit cells. First, as presented in **Figure 2a**, the intense π-π stacking peak of Y6 is concentrated along the q_z axis; therefore, the Y6 molecules within the unit cell should possess

a predominant face-on orientation with the molecular backbone horizontally aligned with respect to the substrate. In addition, due to the averaged π-π distance of 3.41 Å (q_z = 1.84 Å^{-1}, **Figure S2d**), the unit cell should fit four face-on oriented Y6 molecules along the **b** axis. The molecular architectures of a single Y6 and of typical Y6 dimers have been proposed in previous theoretical calculations[20], which are summarized in **Figure S5**. Based on the resolved lattice constants and the reported dimer configurations, we propose the following arrangement of the four Y6 molecules within the unit cell, as illustrated in **Figure 2b-e**: From bottom to top of the unit cell, the configurations of Y6 dimers are "arm-chair", "zig-zag" and "arm-chair" with terminal-terminal (TT) overlap of the end groups. Between neighboring unit cells, the Y6 molecules are connected through "herringbone"-shaped core-core and terminal-terminal (CC-TT) overlaps, as well as TT dimer configurations. Periodic lattice structure can then be appropriately formed by extending the unit cell along the crystallographic primary axis directions. Since in-plane anisotropy of the crystallites in thin film may cause different GIWAXS reflections[42], here we further measured GIWAXS of PM6:Y6 blend film with various azimuth angles of beam incidence. As presented in **Figure S6**, changing the azimuth angle of beam incidence leads to identical GIWAXS patterns, which confirms the in-plane isotropy of thin films fabricated with spin-coating. Therefore, the crystalline structure of Y6 we resolved from GIWAXS pattern should indeed represent its crystal-structure in BHJ active layer.

Figure S7 illustrates that the crystalline structure of Y6 in BHJ active layer we found in this work is notably different from its single crystal[32]. For example, Y6 crystals in thin film

exhibits a characteristic square-shaped lattice along in-plane direction (**Figure S7a**), distinct from the rectangular-like lattice of the single crystal (**Figure S7b**). Essentially, the different crystal lattices will lead to varied packing densities as well as distinctive types and distributions of packing-motifs. These packing features of Y6 crystals should directly impact its ultimate device performance, e.g. exciton diffusion, charge generation and transport, etc.

2.2 Molecular dynamics simulations

As demonstrated above, it is clear that the solvent additive CN impacts the crystal packing of Y6 in the active layer, a feature that has not been reported to date. Although the influence of solvents on the single-crystal structure of Y6 has been highlighted before[33], the crystallization mechanism of Y6 in a thin film in the presence of an additive is still unclear. Therefore, we choose to investigate at the molecular level how CN can influence the crystal structure of Y6 in a thin film, via atomistic molecular dynamics (MD) simulations. We note that the MD simulations primarily consider Y6 and the additives but do not include the solvent CF, which is due to the fact that while the solvent additives with high boiling point (~ 300 °C at one atmosphere) can remain at least partially in the thin film after spin coating, the solvent CF with much lower boiling point (~ 65 °C at one atmosphere) tends to evaporate quickly during film casting. Thus, in fact, our MD simulations try to understand the crystallization mechanism of Y6 during film casting and after the solvent volatilized.

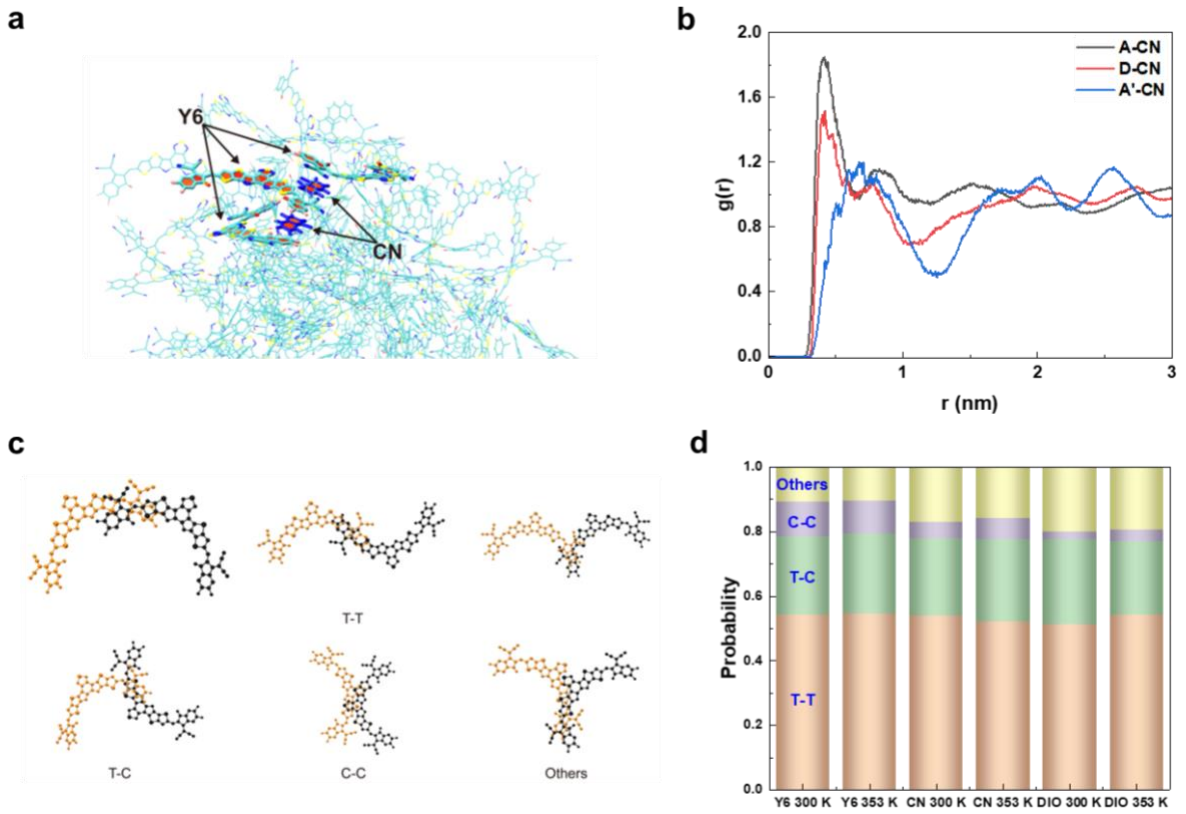

Figure 3. Molecular dynamics simulations. (a) Illustration of the molecular dynamics results for Y6 with CN additive. **(b)** Radial distribution function g(r) data for Y6 with CN at 353 K. The labels for the Y6 moieties are shown in **Figure 1a**. **(c)** Examples of Y6 dimers and **(d)** Corresponding probability distributions under various temperature and additive conditions.

As shown in **Figure 3a** and **Figure S8**, in the Y6/CN mixture, in addition to the typical π-π packings among the Y6 end groups, there also exist π-π interactions between CN and the Y6 end groups, which is confirmed by the radial distribution function (RDF) g(r) data (**Figure 3b** and **Figure S9-10**); here, a higher g(r) peak implies a larger packing density at a given distance r. As presented in **Figure S9**, at the local level, the g(r) intensity between Y6 and CN is largest at distance of ~ 0.4 nm at both 300 K and 353 K, which is in the range of π-π stacking distances. Further calculations reveal that it is the g(r) intensity between CN and the end group (A moiety) of Y6 that is strongest compared to the other moieties (**Figure 3b** and **Figure S10**), implying the π-π interactions mainly originate from CN and the end groups of Y6. MD simulations were

also conducted for pure Y6 and the mixture of Y6 with another additive 1,8-diiodoctane (DIO) for comparison (**Figure S11-13**). There are no additional interactions in the Y6/DIO mixture, which is attributed to the alkyl nature of DIO instead of the aromatic nature of CN. We note that π-π peak of Y6 pure film with CN presents an additional shoulder around 1.5 $Å^{-1}$, which is absent in Y6 pure films without additive or with DIO (**Figure S1d** and **S2d**). This feature might originate from π-π interactions between CN and Y6 end groups.

As presented in **Figure S14**, the calculated interaction energies (sum of the electrostatic and van der Waals forces) between CN and Y6 are also larger than between DIO and Y6. We note that the interaction energies between Y6 molecules in the existence of CN or DIO are rather similar, suggesting that the interactions between CN molecules and Y6 end groups are not detrimental to the self-assembly of Y6 molecules. We hypothesize that the additional π-π interactions induced by the conjugated nature of CN act as a bridge to gather Y6 molecules pre-aligned in the π-π stacking direction in solution and can thus induce the formation of a highly ordered crystalline packing structure during film formation, as seen from the GIWAXS measurements. It is noticed from **Figure S14** that the interactions among Y6 molecules themselves are obviously stronger than that between Y6 and CN molecules. Thus, in the Y6 crystallites of final film, it is assumed that the crystallized Y6 molecules are dominant species although there are still some additives left over (due to the boiling point of ~ 300 °C at one atmosphere). A schematic illustration of the role of the CN additive in the crystallization of Y6 is given in **Figure S15**.

To confirm that coupling between CN and IC-2F end groups of Y6 indeed exists and plays an important role in the crystallization of Y6, the effects of CN on other Y-series molecules with and without IC terminals are further estimated. First, GIWAXS measurements are conducted for neat films of BTP-4Cl (**Figure S16a**) whose end groups (IC-2Cl) are similar with that (IC-2F) of Y6. As presented in **Figure S16c**, thin film processed with CN additive exhibits GIWAXS patterns with discrete and sharp scattering peaks in small-q region, which are similar with the phenomenon of Y6 with CN (**Figure S1-2**), thus indicating that the interactions between CN and IC end groups should generally exist in the Y-series acceptors with similar IC end groups. Then, we have also measured the GIWAXS of another Y-series NFA named BTPR (**Figure S17a**), which has quite different end groups. As presented in **Figure S17b-c**, neat films of BTPR with and without CN show almost identical GIWAXS patterns, distinct from the case of Y6 (**Figure S1-2**), suggesting that there should be no characteristic interactions between CN and BTPR that has no IC-2F end groups. Therefore, it is now evident experimentally that it is the coupling between CN and IC end groups that induces the long-range structure order. Furthermore, Li et al. recently reported that L8-BO thin films added with a naphthalene derivative FN present significantly enhanced structure order in GIWAXS pattern and AFM images[43]. This further confirms that the crystallization enhancement can be generalized to other naphthalene derivatives as the additive. Moreover, we notice that chlorobenzene (CB) with single aromatic ring generally works as a solvent for organic photovoltaic systems and Y6 in CB-processed thin films was found of low crystallinity and poor orientation ordering[32], which suggests that CB can't enhance the crystallization of Y6 as CN does. It has also been reported that solid additive anthracene is highly crystalline and can

restrict the over-aggregation of Y6 molecules in blend film[44], thus implying that naphthalene's capability to induce crystallization of Y6 is not observed for anthracene either. Therefore, we believe that it is the special molecular size with two aromatic rings that endows naphthalene-derivatives the capability to promote packing of Y6 series NFAs.

We also exploited RDF data to further characterize the interactions between the CN moieties and the end group of Y6; the CN molecule is considered as two moieties, one corresponding to the chlorine-substituted benzene ring moiety (CN1) and the other to the unsubstituted benzene ring moiety (CN2); the end group of Y6 is labeled as A1 (difluoro-benzene) and A2 (substituted five-membered ring) moieties (see **Figure S18**). It is found that the A2-CN1 (or CN2) g(r) intensity is the largest among all moiety pairs (**Figure S19**), indicating preferential interactions between A2 and CN, especially CN1. This result suggests that, besides the conjugated rings of CN and the end groups of Y6, the cyano-groups in the terminal groups of Y6 and the halogen substituents in the conjugated additives may also contribute to the additional interactions between Y6 and CN. Considering that most Y-series NFAs have similar end groups, the characteristic interaction found between CN and Y6 end groups is expected to be a universal driving force to promote crystallization of other Y-series molecules, thus providing a good level of guidance for future molecular design of NFAs and additives, on the way towards the ideal molecular interactions and crystalline packing of the NFAs.

As the configurations of the side chains can possibly also affect the packing of the NFA

molecules via steric hindrance effects[40], we evaluated the orientation distributions of the Y6 side chains with various additive conditions based on the above MD simulation results. As shown in **Figure S20**, we define the normal vector of the end group as the main direction and then consider the angle distributions of the various side chains, evaluated over all Y6 molecules in the MD box (**Figure S21-22**). In the case of pure Y6 without additive, the probabilities for all three types of side chains to appear on either side of the end group are rather similar. Interestingly, for the case of Y6 with CN or DIO, the linear side chains tend to appear on only one side of the end group, unlike the branched long chains or branched short chains, which have no preferential orientation around the end group. This specific distribution of the linear side chains may also facilitate an ordered packing of the Y6 molecules by reducing steric hindrance, which is consistent with the more efficient charge transport in devices based on PM6:Y6 with CN or DIO, as discussed below.

Since both the crystalline and amorphous regions of Y6 in the thin film actually consist of various dimers, which have a significant impact not only on the formation of crystalline structure but also on the overall transport properties of the active layer[20,22], we further investigated the influence of the additives on the dimer configurations by quantifying the probability distributions of various dimers. **Figure 3c** presents the four typical configurations of dimers found in the MD simulations: (i) terminal-terminal (T-T) configurations; (ii) core-terminal (C-T) configurations; (iii) core-core (C-C) configurations; and (iv) other configurations among which the core/core-terminal/terminal (CC-TT) overlapping configuration is the most representative. Zoom in on the interacting parts of the Y6 dimers can

be found in **Figure S23**. As shown in **Figure 3d**, the incorporation of solvent additives indeed impacts on the population distributions of the Y6 dimers. Although the proportion of T-T configuration is the largest (~ 50 %) and similar for all six different cases we considered, the case of Y6 with DIO leads to an obvious decrease in the proportion of the C-C configuration. According to a previous report, the C-C interactions contribute significantly to large electronic coupling for exciton transport[22]; here, the decreased proportion of C-C configurations for Y6 with DIO can result in slower exciton diffusion rates, which is confirmed by the transient absorption data on PM6:Y6 blend films in the next section. Moreover, as displayed in **Table S1-2**, it is found that for the cases of Y6 with the CN additive at 300 K and 353 K, the proportion ratio of CC-TT to T-T configurations (~ 1:3) is close to that of the molecular arrangement we proposed above for the unit cell of Y6, which confirms its validity.

According to previous reports, smaller π-π stacking distances between moieties of neighboring molecules can result in larger electronic couplings within the dimers, which would contribute directly to superior transport properties in the active layer[38]. Based on the MD simulation results, we calculated the statistical π-π stacking distances for CT and TT dimers that account for the majority of Y6 dimer configurations. As presented in **Figure S24**, at both 300 K and 353 K, Y6 with the CN additive has the smallest packing distance compared to pure Y6 and Y6 with DIO, which is also consistent with the trends in π-π peak positions observed by GIWAXS below (**Figure S1-2** and **Table S3**). This confirms once more the fundamental influence of the CN additive on the crystalline packing of Y6 and consequently on the device characteristics.

2.3 Correlation with device characteristics and photophysical properties

In the following, we elucidate the impact that the Y6 crystal structure we have uncovered in the active layer thin film has on the device characteristics. We have considered two additional common device fabrication conditions: without additive and with 0.5vol% DIO. The GIWAXS patterns of the Y6 films without additive or with 0.5vol% DIO (**Figure S1-2**) present q_r profiles with similar peak positions at 0.21 $Å^{-1}$, 0.28 $Å^{-1}$ and 0.42 $Å^{-1}$; this implies the existence of a similar crystalline packing motif for Y6 in these films despite of a much lower degree of ordering. The π-π peaks in these two films (**Figure S1d**) appear at q_z = 1.75 $Å^{-1}$ (*d*-spacing = 3.59 Å), a smaller value compared with the π-π peak position of the CN-processed film (q_z =1.79 $Å^{-1}$, *d*-spacing = 3.51 Å); thus, CN appears to promote a tighter molecular packing and a better ordered crystalline packing structure for Y6. Furthermore, the π-π peak of the film without additive is the weakest and concentrated along the q_z axis, while that of the DIO-processed film is more intense but spans a larger polar angle. This suggests that the film without additive has less crystallinity but favorable face-on orientation while the DIO-processed film has higher crystallinity but more random orientation; in contrast, CN can simultaneously improve both the long-range ordering and the orientation order of Y6. The GIWAXS patterns of the PM6:Y6 blend films fabricated with the same conditions (**Figure S25**) show the same trends as the neat films. GIWAXS of the pure PM6 films with various additives and the grazing-incidence transmission small-angle X-ray scattering (GTSAXS)[45] of the PM6:Y6 blend films have been measured and displayed in **Figure S26-27**; the data demonstrate that the crystalline packing in PM6 and the nanophase separation in PM6:Y6 are not altered notably under these

three device fabrication conditions. Specifically, the GTSAXS fitting results in **Figure S27** shows that compared with the control BHJ, the 3D domain sizes of pure Y6 phase in experiment BHJ phase do not change notably with the incorporation of various additives, only slight shrinkage of in-plane domain size is observed for the blend film with DIO. Therefore, the device characteristics we describe below can be mainly attributed to the distinct crystalline packing of Y6 in the active layer.

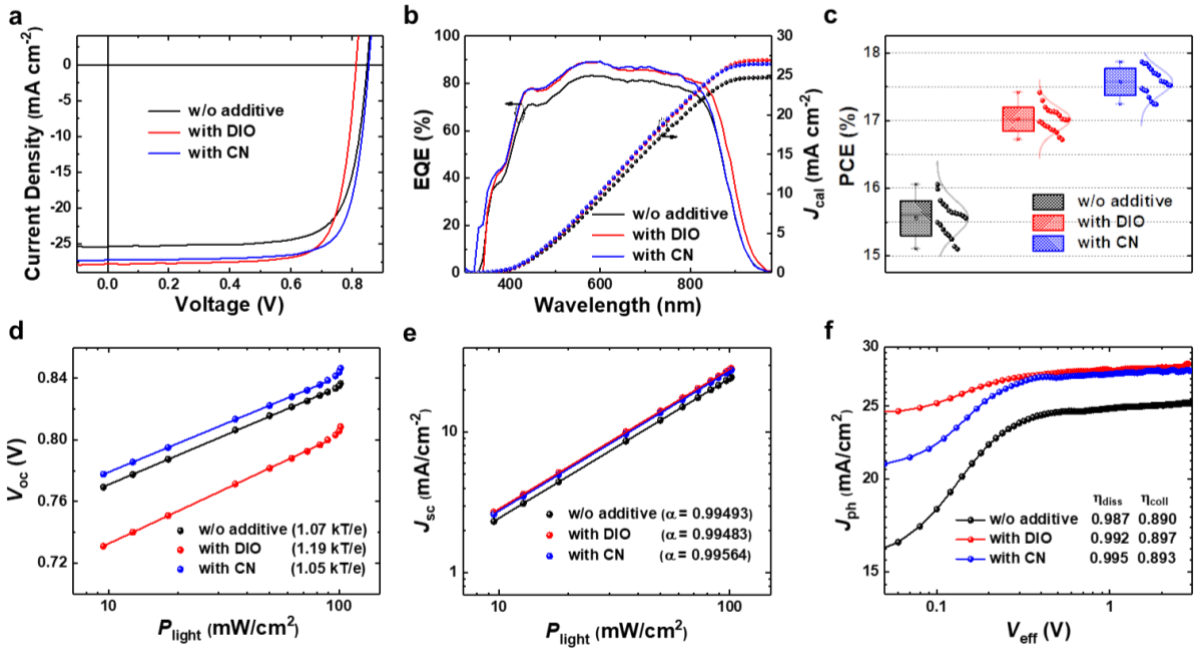

Figure 4. Device characteristics of PM6:Y6. (a) *J*-*V* curves of OSCs based on PM6:Y6 blends prepared with various additive conditions. **(b)** EQE curves, **(c)** PCE distribution, dependence of **(d)** V_{oc} and **(e)** J_{sc} on light intensity and **(f)** photogenerated current density versus effective voltage curves for the corresponding devices.

Table 1. Photovoltaic parameters of OSCs based on various PM6:Y6 blends. Average parameters with standard deviation in parentheses were obtained from 10 individual devices.

Devices	V_{oc} (V)	J_{sc} (mA cm^{-2})	FF (%)	PCE (%)	J_{cal}[a] (mA cm^{-2})
w/o additive	0.849 (0.848±0.001)	25.36 (24.86±0.36)	74.62 (73.83.±0.82)	16.05 (15.56±0.25)	24.73
with DIO	0.812 (0.807±0.002)	27.77 (27.61±0.15)	77.10 (76.33±0.36)	17.41 (17.02±0.17)	26.94
with CN	0.854 (0.849±0.003)	27.23 (27.17±0.29)	77.20 (76.27±0.84)	17.87 (17.57±0.20)	26.47

[a] Integrated current densities from EQE curves.

Figure 4a and **Table 1** present the device characteristics of OSCs based on PM6:Y6. Compared to the device without additive, the J_{sc} and *FF* values are simultaneously enhanced for devices with 0.5vol% CN or DIO additives, which contributes to an increase in PCE. The improvement in J_{sc} and FF for the devices with CN are essentially due to the highly ordered crystal structure of the Y6 phase revealed above, which results in better charge generation and transport efficiency. The solvent additive DIO, which has a high boiling point, can extend the evaporation time of the solvent chloroform during film casting; this contributes to increase the crystallization time of Y6 and improve its crystallinity in blend films, as evidenced by the higher intensity of the q_r peak at 0.28 $Å^{-1}$ (**Figure S1-2**) and larger crystalline coherence length (CCL) of π-π stacking (**Table S4**) in the GIWAXS pattern of Y6 with DIO compared with that of Y6 without additive, which should also help enhance J_{sc} and *FF*[31]. Interestingly, compared with the device without additive, the V_{oc} value of PM6:Y6 device with DIO decreases strongly from 0.849 V to 0.812 V, whereas V_{oc} in the device with CN additive increases slightly from 0.849 V to 0.854 V. This opposite trend in V_{oc} is possibly related to the distinct crystal orientations of Y6 induced by the various additives (**Figure S1-2** and **S25**), with the less ordered orientation of Y6 with DIO resulting in increased energetic disorder (as indicated by the larger Urbach energy in **Figure S28**), which thus leads to narrowed bandgap and increased energy loss within the BHJ active layer[18, 46-47] (the energy losses will be discussed in detail in the following section). The integrated J_{sc} values from the EQE spectra of the corresponding devices are highly consistent with the measured values from the *J-V* curves within less than 3% error (**Figure 4b**, **Table 1**), suggesting the reliability of the *J-V* measurements of the devices.

Compared with devices without additive or with CN, the device with DIO has a red-shifted absorption edge (**Figure 4b**), which can originate from a broadened distribution of the density of states caused by the orientational disorder in the Y6 crystallites[31]. We note that the Jsc of devices obtained in this work is relatively higher than previous literatures[32], which might originate from raw materials quality, fabrication skill and thickness variations. The statistical analysis of the PCE values confirms that the PM6:Y6 binary devices fabricated with the CN additive possess superior performance (**Figure 4c**), which is attributed to the simultaneous improvements in J_{sc}, FF, and especially V_{oc}, due to the distinctive long-range ordering and orientation order of Y6 with CN, indicating the direct influence of the Y6 crystalline morphology on the OSC device characteristics. OSCs based on PM6:Y6 with 0.5vol% CN and various D/A ratios were also prepared (**Figure S29** and **Table S5**). It is noticed that when D/A ratio equals 1:2 or 1:4, although the content of donor is highly deficient, the three parameters of the devices (especially Voc) could remain a relatively high level, further illustrating the fundamental effect of Y6 crystallization on the device performances.

Charge recombination in the various devices were evaluated via *J-V* tests under various light intensities (P_{light}). The relationship between V_{oc} and P_{light} is described as $V_{oc} \propto nkT/q\ln(P_{light})$ in which q, k, and T denote the elementary charge, Boltzmann constant, and Kelvin temperature, respectively. As shown in **Figure 4d**, the slopes are fitted to be 1.07, 1.19, and 1.05 kT/q for the OSCs without additive, with DIO, and with CN additive, respectively. These results suggest that the addition of DIO dramatically increases monomolecular recombination while the CN additive tends to suppress those; we can thus expect difference in

the energy loss mechanisms, as will be confirmed below. **Figure 4e** presents J_{sc} vs P_{light} plots for the three cases; compared with the control devices, the devices with DIO exhibit smaller α value and hence more bimolecular recombination. Therefore, the higher Jsc and FF of devices with DIO that contribute to better PCE should mainly be ascribed to the apparently enhanced and wider absorption spectra (**Figure S30**) and increased crystallinity (**Figure S25**, **Table S4**) of PM6:Y6 with DIO.

The charge collection efficiency of the devices has been investigated via the dependence of the photocurrent density (J_{ph}) on the effective internal voltage (V_{int}). The photocurrent density (J_{ph}) is defined as $J_{ph} = J_L - J_D$, where J_L represents the current density under illumination and J_D is the current density in the dark. The charge collection probability (PC) can be calculated according to PC = $J_{ph}/J_{ph,sat}$, where $J_{ph,sat}$ is the saturated photocurrent density at high V_{int} (defined as $V_{int} = V_0 - V$, where V_0 is the voltage when the net current is zero, and V is the applied voltage); η_{diss} and η_{coll} are defined as the PCs under short-circuit and maximum power-output points, respectively, and refer to the exciton-dissociation and charge-collection efficiencies. **Figure 4f** shows the plots between J_{ph} and V_{int}. The η_{diss} and η_{coll} values are simultaneously enhanced for OSCs with DIO or CN compared to the devices without additive, which should again originate from the improved crystallinity and contribute to the higher J_{sc} and FF values in the corresponding OSCs.

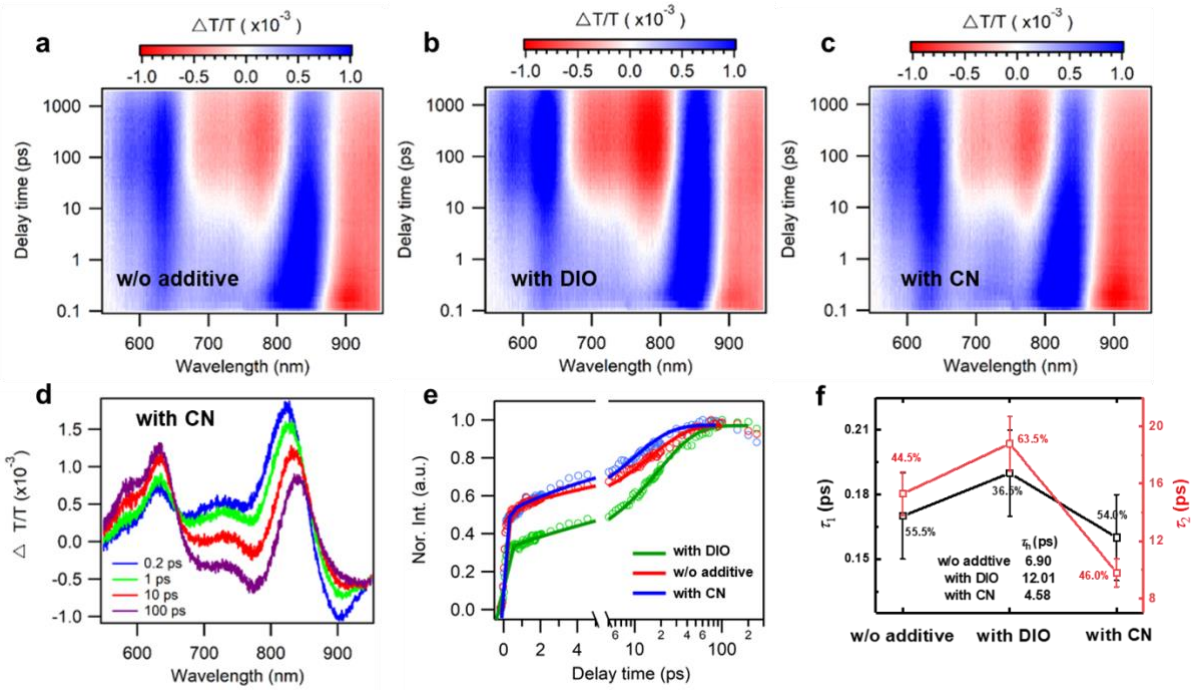

Figure 5. Hole transfer dynamics. Color plots of the TA spectra of PM6:Y6 blends **(a)** without additive, **(b)** with 0.5vol% DIO and **(c)** with 0.5vol% CN under 750 nm excitation. **(d)** TA spectra at various delay times for PM6:Y6 blend film with 0.5vol% CN. **(e)** Hole transfer dynamics of the three blend films. **(f)** Comparisons of τ_1 and τ_2 among various blend films.

We now turn to the impact of the intrinsic crystalline packing structure of Y6 on the fundamental photophysical properties of the OSCs during the photon to electron conversion processes. The hole-transfer kinetics from Y6 to PM6 within the BHJ active layer was studied via transient absorption (TA) spectroscopy, with the Y6 phase exclusively excited by a 750 nm laser excitation. As illustrated in **Figure S31**, similar ground-state bleaching (GSB) signals at ~ 850 nm are observed for the Y6 pure films under various additive conditions. For the PM6:Y6 blend films, the corresponding bleaching peaks of Y6 also appear immediately after photoexcitation (**Figure 5a-d**, **Figure S32**). With an increase in delay time, the bleaching signal of Y6 gradually decays, while a new bleaching peak arises at ~ 640 nm, which is attributed to the donor PM6 according to its absorption spectrum. The evolution of the two peaks is indicative of the hole transfer process from Y6 to PM6. The hole transfer kinetics of the

different PM6:Y6 blend films were analyzed from the profiles of the PM6 bleaching peak intensity (I) versus delay time (t) taken from the wavelength of 608 nm. Typically, the hole-transfer process consists of an ultrafast hole-transfer process and a diffusion-mediated process, which can be fitted by a biexponential function:

$$I = A_1 \exp\left(-\frac{t}{\tau_1}\right) + A_2 \exp\left(-\frac{t}{\tau_2}\right) \quad (1)$$

with lifetimes τ_1 and τ_2 and pre-factors A_1 and A_2. The ultrafast charge-transfer process indicated by τ_1 should be attributed to D/A interfacial charge-transfer processes while the NFA exciton diffusion mediated process described by τ_2 is generally dominated by the BHJ morphologies[48-49]. As illustrated in **Figure 5e-f**, the PM6:Y6 blend film with DIO appears to present simultaneously the largest time constants τ_1 and τ_2. In contrast, PM6:Y6 blend film with CN exhibits the shortest time constants for both τ_1 and τ_2. The average hole-transfer times (τ_h) are calculated with τ_1, τ_2 and their respective proportions (A_1, A_2); as illustrated in **Figure 5f**, the τ_h value for the PM6:Y6 blend film with DIO is about 2 ~ 3 times longer than that of the blend film with CN. The remarkable hole transfer efficiency of the blend film with the CN additive is expected to be related to the molecular ordering of Y6 formed with the assistance of CN, as confirmed by the molecular dynamics simulations discussed above for the dimer distributions; this larger extent of molecular ordering allows faster exciton diffusion rates, while the much slower hole-transfer rate of PM6:Y6 with DIO is possibly due to the less ordered orientations of Y6 crystallites. Overall, the addition of CN promotes the molecular ordering of Y6, which enhances J_{sc} in the device via an improvement in the charge-transfer dynamics (rather than via a red-shift of the absorption edge), unlike the situation in the device with DIO.

According to the results of earlier calculations, the distinct molecular packing of Y6 favors not only significant exciton couplings between adjacent molecules, which facilitates the exciton diffusion process, but also reduces exciton-vibration couplings and generally leads to slower non-radiative decay rates[20]. Now, we seek to further characterize the specific energy loss mechanisms in the OSCs. **Figure S33** and **Table S6** collect the detailed energy loss analysis of the relevant devices. First, compared to the devices without additive, the addition of CN increases the bandgap (Eg) slightly from 1.400 eV to 1.405 eV, and the addition of DIO decreases the bandgap from 1.400 eV to 1.385 eV, which should contribute to an improvement in J_{sc} but also a lowering of V_{oc} for devices prepared with DIO. We find that the Voc variations of devices with additives have the same trend as their bandgaps; this indicates that the varied distributions of density of states caused by orientational ordering might also influence the band gaps, thus leading to the distinctive Voc of devices with additives. In addition, the radiative energy losses above (ΔE_1) and below (ΔE_2) bandgap are similar for the various devices. As for the non-radiative energy loss (ΔE_3), compared to the devices without additive, while there is almost no change after addition of CN, the incorporation of DIO significantly increases the ΔE_3; this can be attributed to the Y6 intrinsic dimer distributions in the presence of DIO, as shown by the MD simulations, as well as to the lower orientational order (**Figure S1-2** and **S25**) that causes increased energetic disorder[46-47]. These results confirm the profound impact of molecular packing on the non-radiative voltage loss.

3. Conclusion

The intrinsic crystalline structure of Y6 in BHJ active layer of an actual solar cell device has been resolved in detail via GIWAXS measurements, which reveal a highly ordered 3D molecular network that is basically different from its single-crystal structure, thus allowing a new understanding on crystalline packing of Y6 in BHJ active layer. The use of 1-chloronaphthalene (CN) as a solvent additive is found to play a crucial role in the formation of a highly ordered crystalline structure of Y6 in thin films. MD simulations show that the intermolecular interactions between the CN molecules and the Y6 end groups are the underlying driving force that facilitates the ordered packing of Y6 and ultimately results in the distinct crystalline structure that Y6 adopts in thin films. Such π-π interactions are also found universally existed between naphthalene derivative and IC terminals of Y-series NFAs, thereby providing a mechanism to control crystalline packing of other Y6 analogues. The specific crystalline packing structure of Y6 we have uncovered is shown to lead to fast charge generation and efficient carrier transport while maintaining low energy losses, which accounts for the superior device performances, indicating the potential of device optimization through fine tuning the NFA crystalline structures.

Experimental Section

***Materials*:** PM6, Y6 and BTP-4Cl were purchased from Solarmer Material Inc. (China). BTPR was synthesized according to literature report[47]. 1,8-diiodooctane (DIO), 1-chloronaphthalene (CN) and chloroform (CF) were purchased from Sigma-Aldrich. All other materials were purchased and used as received.

***X-ray scattering measurements*:** GIWAXS measurements were carried out with a Xeuss 2.0

SAXS/WAXS laboratory beamline using a Cu X-ray source (8.05 keV, 1.54 Å) and a Pilatus3R 300K detector. The incidence angle is 0.2°. The thin film samples (including pure and blend films) were prepared on Si wafer substrates by spin coating the precursor solutions (in CF) with certain amount of solvent additive; some of the thin film samples were thermally annealed for 10 minutes at 80°C. GTSAXS measurements were performed at beamline BL19U2 of the National Facility for Protein Science Shanghai (NFPS) at Shanghai Synchrotron Radiation Facility (SSRF); the methodology we followed is the same as that described in the literature [44].

***Molecular dynamics simulations*:** The all-atom molecular dynamics simulations were carried out with the GROMACS2021.2 package[50]. The optimized potentials for liquid simulations-all atom (OPLS-AA) force field[51-52], which is a well-established force field for organic π-conjugated molecules, was adapted for the Y6 molecule from the report of Kupgan and co-workers[22] and for additives 1-chloronaphthalene (CN) and 1,8-diodooctane (DIO). Partial charges for all the molecules were obtained by the restrained electrostatic potential (RESP) fitting method. The Density Functional Theory (DFT) calculations were performed with Gaussian 16[53].

The neat films were simulated from isothermal-isobaric ensemble molecular dynamics (NPT-MD). The initial models were built by randomly placing additives and Y6 molecules in cubic cells with an extremely low density of ~ 0.1 g/cm^3. The cells of [19.3 × 19.3 × 19.3] nm^3, [27.2 × 27.2 × 27.2] nm^3 and [28.5 × 28.5 × 28.5] nm^3, included 300 Y6 molecules (total of 56100 atoms), 2078 CN and 600 Y6 molecules (total of 149604 atoms), and 1416 DIO and 600 Y6 molecules (total of 149016 atoms), respectively. The specific number ratios of Y6 and additive molecules were derived from the concentration of Y6 and the volume fraction of

additives in the actual precursor solutions.

Following the random placement of molecules, NPT-MD was performed under 1 atm. Two temperatures were simulated: 353 K, which is consistent with the experimental annealing temperature, and room temperature 300 K. To simulate the experimental annealing process, MD simulations were performed by going from 353 (30 ns) to 300 K (30 ns), where 353 K is the annealing temperature, with a cooling rate from 353 to 300 K of 10 K/ns. For the case of room temperature, 65 ns of NPT-MD was performed at 300 K to equilibrate the system. The box size and density were analyzed from the last 10 ns of the NPT-MD. The final box size of each cell is [8.657 × 8.657 × 8.657], [11.874 × 11.874 × 11.874], [11.796 × 11.796 × 11.796] nm^3 for pure Y6 without additive, with additive CN and, with additive DIO at 300 K and [8.553 × 8.553 × 8.553], [11.861 × 11.861 × 11.861], [11.780 × 11.780 × 11.780] nm^3 for the three thin films at 353 K, respectively. The final system density was 1.117, 1.200, and 1.407 g/cm^3 for pure Y6 without additive, with additive CN, and with additive DIO at 300 K and 1.159, 1.205, and 1.410 g/cm^3 for the three thin films at 353 K, respectively. The equilibrated densities are consistent with the experimental values.

The LINCS algorithm was applied to constrain the covalent bonds with H-atoms[54]. The time step of the simulations was 1.0 fs. All the simulations were performed in periodic boundary conditions. Pressure and temperature were controlled with the Parrinello-Rahman barostat[55] and Nose-Hoover thermostat[56]. The cut-off of the non-bonded interactions was set to 12 Å. The particle mesh Ewald (PME) method was used to calculate the long-range electrostatic interactions[57]. The graphics and visualization analyses were processed with the Visual Molecular Dynamics (VMD) program[58].

***Fabrication and characterization of OSC devices*:** The conventional structure ITO/PEDOT:PSS/PM6:Y6/PFN-Br/Ag was used to prepare devices. The PEDOT:PSS layer was spin-coated from its aqueous solution on precleaned ITO glass, then baked at 130 ^{o}C in air for 20 min. PM6:Y6 solutions (17.6 mg/ml in CF) with 0.5vol% different solvent additives (DIO or CN) were prepared and spin-coated on the PEDOT:PSS layer at 2000 rpm in N_2-filled glove box, then followed with thermal annealing at 80 ˚C for 10 min. After that, a poly(9,9-bis(3'-(N,N-dimethyl)-N-ethylammoinium-propyl-2,7-fluorene)-alt-2,7-(9,9-dioctylfluorene))dibromide (PFN-Br) layer with a thickness of ~ 5 nm was spin-coated as the electron transporting layer and the Ag (ca. 100 nm) were thermally evaporated as the top electrode. The devices have an active area of 9.25 mm^2, as defined by the overlapping area of the ITO and Ag electrodes. A mask with an area of 5.979 mm^2 (certified by National Institute of Metrology, China) was used to measure the efficiencies. The device parameters were measured via the solar simulator (SS-F5-3A, Enlitech) along with AM 1.5 G spectra at 100 mW/cm^2, which were calibrated by the certified standard silicon solar cell (SRC-2020, Enlitech) with KG-2 filter. Devices were tested in an N_2-filled glovebox. The scan direction is −0.2 to 1.2 V, with a scan step of 0.01 V and dwell time of 1 ms. The EQE spectra were tested by using the solar-cell spectral-response measurement system (RE-R, Enlitech).

***Transient absorption spectroscopy*:** For femtosecond transient absorption spectroscopy, the fundamental output from a Yb:KGW laser (1030 nm, 220 fs Gaussian fit, 100 kHz, Light Conversion Ltd) was split into two light beams. One was sent to a NOPA (ORPHEUS-N, Light Conversion Ltd) to produce a specific wavelength for the pump beam (here, we use 750 nm, the excitation fluence is 5 $\mu J/cm^2$); the other was focused onto a YAG plate to generate a white

light continuum as probe beam. The pump and probe beams overlapped on the sample at a small angle less than 10°. The transmitted probe light from the sample was collected by a linear CCD array. Then, we evaluated the transient differential transmission signals from the equation shown below:

$$\frac{\Delta T}{T} = \frac{T_{pump-on} - T_{pump-off}}{T_{pump-off}} \qquad (2)$$

***FTPS-EQE measurement*:** The FTPS-EQE was measured with a Vertex 70 from Bruker Optics, which was equipped with a quartz tungsten halogen lamp, quartz beam-splitter, and external detector option. A low-noise current amplifier (SR570) was used to amplify the photocurrent produced under illumination of the solar cells, with light modulated by a Fourier transform infrared spectrometer (FTIR). The output voltage of the current amplifier was fed back into the external detector port of the FTIR to use the FTIR software to collect the photocurrent spectra.

***EQE$_{EL}$ measurement*:** The EQE$_{EL}$ was recorded with an in-house system comprising a Hamamatsu silicon photodiode 1010B, Keithley 2400 source meter (for supplying voltages and recording injected currents), and Keithley 485 picoammeter (for measuring the emitted light intensity).

Data availability

The data reported in this article are available upon request.

References

1 H. Chen, R. Zhang, X. Chen, G. Zeng, L. Kobera, *Nat. Energy*, 2021, **6**, 1045-1053.

2 X.-K. Chen, D. Qian, Y. Wang, T. Kirchartz, W. Tress, H. Yao, J. Yuan, M. Hülsbeck,

M. Zhang, Y. Zou, Y. Sun, Y. Li, J. Hou, O. Inganäs, V. Coropceanu, J.-L. Bredas & F. Gao, *Nat. Energy,* 2021, **6**, 799-806.

3 Y. Firdaus, V. Corre, S. Karuthedath, W. Liu, A. Markina, W. Huang, S. Chattopadhyay, M. Nahid, M. Nugraha, Y. Lin, A. Seitkhan, A. Basu, W. Zhang, I. McCulloch, H. Ade, J. Labram, F. Laquai, D. Andrienko, L. Koster & T. Anthopoulos, *Nat. Commun.*, 2020, **11**, 5220.

4 C. Li, J. Zhou, J. Song, J. Xu, H. Zhang, X. Zhang, J. Guo, L. Zhu, D. Wei, G. Han, J. Min, Y. Zhang, Z. Xie, Y. Yi, H.Yan, F.Gao, F. Liu & Y. Sun, *Nat. Energy*, 2021, **6**, 605-613.

5 Y. Li, Y. Guo, Z. Chen, L. Zhan, C. He, Z. Bi, N. Yao, S. Li, G. Zhou, Y. Yi, Y. Yang, H. Zhu, W. Ma, F. Gao, F. Zhang, L. Zuo and H. Chen, *Energy Environ. Sci.*, 2022, **15**, 855-865.

6 J. Yuan, Y. Zhang, L. Zhou, G. Zhang, H. Yip, T. Lau, X. Lu, C. Zhu, H. Peng, P. Johnson, M. Leclerc, Y. Cao, J. Ulanski, Y. Li, Y. Zou, *Joule*, 2019, **3**, 1140-1151.

7 L. Zhan, S. Li, Y. Li, R. Sun, J. Min, Z. Bi, W. Ma, Z. Chen, G. Zhou, H. Zhu, M. Shi, L. Zuo, H. Chen, *Joule*, 2022, **6**, 662-675.

8 L. Zhan,S. Li,X. Xia,Y. Li,X. Lu, L. Zuo, M. Shi, H. Chen. *Adv. Mater.*, 2021, **33**, 2007231.

9 Z. Zheng, J. Wang, P. Bi, J. Ren, Y. Wang, Y. Yang, X. Liu, S. Zhang, J. Hou, *Joule*, 2022, **6**, 171-184.

10 R. Sun, W. Wang, H. Yu, Z. Chen, X. Xia, H. Shen, J. Guo, M. Shi, Y. Zheng, Y. Wu, W. Yang, T. Wang, Q. Wu, Ya. Yang, X. Lu, J. Xia, C. Brabec, H. Yan, J. Min, *Joule*, 2021, **5**, 1548-1565.

11 S. Li, L. Zhan, N. Yao, X. Xia, Z. Chen, W. Yang, C. He, L. Zuo, M. Shi, H. Zhu, X. Lu, F. Zhang & H. Chen, *Nat. Commun.*, 2021, **12**, 4627.

12 Y. Lin, J. Wang, Z. Zhang, H. Bai, Y. Li, D. Zhu, X. Zhan, *Adv. Mater.*, 2015, **27**, 1170-1174.

13 G. Han, T. Hu, Y. Yi, *Adv. Mater.*, 2020, **32**, 2000975.

14 G. Han and Y. Yi, *Acc. Chem. Res.*, 2022, **55**, 869-877.

15 J. Kim, T. Schembri, D. Bialas, M. Stolte, F. Würthner. *Adv. Mater*., 2022, **34**, 2270169.

16 W. Li, M. Chen, J. Cai, E. Spooner, H. Zhang, R. Gurney, D. Liu, Z. Xiao, D. Lidzey, L. Ding, T. Wang, *Joule*, 2019, **3**, 819-833.

17 J. Mai, Y. Xiao, G. Zhou, J. Wang, J. Zhu, N. Zhao, X. Zhan, X. Lu, *Adv. Mater*., 2018, e1802888.

18 L. Perdigón-Toro, L. Phuong, F. Eller, G. Freychet, E. Saglamkaya, J. Khan, Q. Wei, S. Zeiske, D. Kroh, S. Wedler, A. Köhler, A. Armin, F. Laquai, E. Herzig, Y. Zou, S. Shoaee, D. Neher, *Adv. Energy Mater.*, 2022, **12**, 2103422.

19 L. Ye, K. Weng, J. Xu, X. Du, S. Chandrabose, K. Chen, J. Zhou, G. Han, S. Tan, Z. Xie, Y. Yi, N. Li, F. Liu, J. Hodgkiss, C. Brabec & Y. Sun, *Nat. Commun.*, 2020, **11**, 6005.

20 G. Zhang, X.-K. Chen, J. Xiao, P. Chow, M. Ren, G. Kupgan, X. Jiao, C. Chan, X. Du, R. Xia, Z. Chen, J. Yuan, Y. Zhang, S. Zhang, Y. Liu, Y. Zou, H. Yan, K. Wong, V. Coropceanu, N. Li, C. Brabec, J.-L. Bredas, H. Yip & Y. Cao, *Nat. Commun.*, 2020, **11**, 3943.

21 X. Zhang, C. Li, J. Xu, R. Wang, J. Song, H. Zhang, Y. Li, Y. Jing, S. Li, G. Wu, J. Zhou, X. Li, Y. Zhang, X. Li, J. Zhang, C. Zhang, H. Zhou, Y. Sun, Y. Zhang, *Joule*, 2022, **6**, 444-457.
22 G. Kupgan, X. Chen, J. Brédas, *Mater. Today Adv.*, 2021, **11**, 100154.
23 R. Wang, J. Yuan, R. Wang, G. Han, T. Huang, W. Huang, J. Xue, H. Wang, C. Zhang, C. Zhu, P. Cheng, D. Meng, Y. Yi, K. Wei, Y. Zou, Y. Yang, *Adv. Mater.*, 2019, **31**, 1904215.
24 J. Yuan, T. Huang, P. Cheng, Y. Zou, H. Zhang, J. Yang, S. Chang, Z. Zhang, W. Huang, R. Wang, D. Meng, F. Gao & Y. Yang, *Nat. Commun.*, 2019, **10**, 570.
25 J. Yuan, Y. Zhang, L. Zhou, C. Zhang, T. Lau, G. Zhang, X. Lu, H. Yip, S. So, S. Beaupré, M. Mainville, P. Johnson, M. Leclerc, H. Chen, H. Peng, Y. Li, Y. Zou, *Adv. Mater.*, 2019, **31**, 1807577.
26 H. Liang, H. Chen, P. Wang, Y. Zhu, Y. Zhang, W. Feng, K. Ma, Y. Lin, Z. Ma, G. Long, C. Li, B. Kan, Z. Yao, H. Zhang, X. Wan, Y. Chen, Adv. Funct. Mater., 2023, 17: 2301573.
27 P. Cheng, G. Li, X. Zhan, Y. Yang, *Nat. Photon.*, 2018, **12**, 131-142.
28 S. Zhang, Y. Qin, J. Zhu, J. Hou, *Adv. Mater.*, 2018, **30**, 1800868.
29 W. Zhao, S. Li, H. Yao, S. Zhang, Y. Zhang, B. Yang, and J. Hou, *J. Am. Chem. Soc.*, 2017, **139**, 7148-7151.
30 G. Li, L. Feng, S Mukherjee, L. Jones, R. Jacobberger, W. Huang, R. Young, R. Pankow, W. Zhu, N. Lu, K. Kohlstedt, V. Sangwan, M. Wasielewski, M. Hersam, G. Schatz, D. DeLongchamp, A. Facchetti, and T. Marks, *Energy Environ. Sci.*, 2022, **15**, 645-659.
31 J. Xu, S. Jo, X. Chen, G. Zhou, M. Zhang, X. Shi, F. Lin, L. Zhu, T. Hao, K. Gao, Y. Zou, X. Su, W. Feng, A. Jen, Y. Zhang, F. Liu, *Adv. Mater.*, 2022, **34**, e2108317.
32 L. Zhu, M. Zhang, G. Zhou, T. Hao, J. Xu, J. Wang, C. Qiu, N. Prine, J. Ali, W. Feng, X. Gu, Z. Ma, Z. Tang, H. Zhu, L. Ying, Y. Zhang, F. Liu, *Adv. Energy Mater.*, 2020, **10**, 1904234.
33 B. Luginbuhl, P. Raval, T. Pawlak, Z. Du,T. Wang, G. Kupgan, N. Schopp, S. Chae, S. Yoon, A. Yi, H. Kim, V. Coropceanu, J. Brédas, T. Nguyen, G. Reddy, *Adv. Mater.*, 2022, **34**, 2105943.
34 X. Lu, H. Hlaing, D. Germack, J. Peet, W. Jo, D. Andrienko, K. Kremer & B. Ocko, *Nat. Commun.*, 2012, **3**, 795.
35 Y. Xiao, R. Ma, G. Zhou, J. Zhu, T. Lau, S. Dai, J. Rech, N. Zhao, W. You, H. Yan, X. Zhan, and X. Lu, *ACS Appl. Energy Mater.*, 2020, **3**, 10814-10822.
36 Y. Xiao, J. Yuan, G. Zhou, K. Ngan, X. Xia, J. Zhu, Y. Zou, N. Zhao, X. Zhan, and X. Lu, *J. Mater. Chem. A*, 2021, **9**, 17030-17038.
37 J. Wang, X. Jiang, H. Wu, G. Feng, H. Wu, J. Li, Y. Yi, X. Feng, Z. Ma, W. Li, K. Vandewal & Z. Tang, Nat. Commun., 2021, 12: 6679.
38 C. Li, X. Gu, Z. Chen, X. Han, N. Yu, Y. Wei, J. Gao, H. Chen, M. Zhang, A. Wang, J. Zhang, Z. Wei, Q. Peng, Z. Tang, X. Hao, X. Zhang, and H. Huang, *J. Am. Chem. Soc.*, 2022, **144**, 14731-14739.
39 J. Lv, H. Tang, J. Huang, C. Yan, K. Liu, Q. Yang, D. Hu, R. Singh, J. Lee, S. Lu, G. Li, and Z. Kan, *Energy Environ. Sci.*, **14**, 3044-3052 (2021).
40 X. Wang, C. Feng, P. Liu, Z. He, Y. Cao, *Small*, 2022, **18**, 2107106.

41 R. Yu, H. Yao, L. Hong, Y. Qin, J. Zhu, Y. Cui, S. Li & J. Hou, *Nat. Commun*., 2018, **9**, 4645.
42 E. Tsai, Y. Xia, M. Fukuto, Y. Loo, R. Li, *J. Appl. Cryst.* 2021, **54**:1327-39.
43 D. Li, N. Deng, Y. Fu, C. Guo, B. Zhou, L. Wang, J. Zhou, D. Liu, W. Li, K. Wang, and Y. Sun, *Adv. Mater.,* 2022, 2208211.
44 H. Fan, H. Yang, Y. Wu, O. Yildiz, X. Zhu, T. Marszalek, P. Blom, C. Cui, and Y. Li, Adv. Funct. Mater. 2021, **31**, 2103944.
45 X. Xia, T. Lau, X. Guo, Y. Li, M. Qin, K. Liu, Z. Chen, X. Zhan, Y. Xiao, P. Chan, H. Liu, L. Xu, G. Cai, N. Li, H. Zhu, G. Li, Y. Zhu, T. Zhu, X. Zhan, X. Wang & X. Lu, *Nat. Commun.*, 2021, **12**, 6226.
46 J. Yuan, C. Zhang, B. Qiu, W. Liu, S. So, M. Mainville, M. Leclerc, S. Shoaee, D. Neher, Y. Zou, Energy Environ. Sci., 2022, 15, 2806-2818.
47 W. Feng, S. Wu, H. Chen, L. Meng, F. Huang, H. Liang, J. Zhang, Z. Wei, X. Wan, C. Li, Z. Yao, Y. Chen, Adv. Energy Mater., 2022, 12, 2104060.
48 Z. Chen, X. Chen, B. Qiu, G. Zhou, Z. Jia, W. Tao, Y. Li, Y. Yang, and H. Zhu, *J. Phys. Chem. Lett.*, 2020, **11**, 3226-3233.
49 Z. Chen and H. Zhu, *J. Phys. Chem. Lett.*, 2022, **13**, 1123-1130.
50 Y. Zhang, G. Cai, Y. Li, Z. Zhang, T. Li, X. Zuo, X. Lu, Y. Lin, Adv. Mater. 2021, 2008134.
51 M. Abraham, T. Murtola, R. Schulz, S. Páll, J. Smith, B. Hess, E. Lindahl. *SoftwareX*, 2015, **1**, 19-25.
52 W. Jorgensen, J. Rives, *J. Am. Chem. Soc.*, 1988, **110**, 1657-1666.
53 M. Dahlgren, P. Schyman, J. Rives, and W. Jorgensen, *J. chem. Inform. Model.*, 2013, **53**, 1191-1199.
54 Frisch M. J, 2016, Gaussian 16, Revision C.01, Gaussian, Inc., Wallingford CT.
55 B. Hess, H. Bekker, H. Berendsen, J. Fraaije, *J. Comput. Chem.*, 1997, **18**, 1463-1472.
56 M. Parrinello, A Rahman, *J. Appl. Phys.*, 1981, **52**, 7182-90.
57 S. Nosé, *J. Chem. Phys.*, 1984, **81**, 511-9.
58 U. Essmann, L. Perera, M. Berkowitz, T. Darden, H. Lee, and L. Pedersen, *J. Chem. Phys.*, 1995, **103**, 8577-8593.
59 W. Humphrey, A. Dalke, K. Schulten, *J. Mol. Graph.*, 1996, **14**, 33-38.

Acknowledgements

We thank the Research Grants Council (RGC) of Hong Kong (General Research Fund No. 14303519), and CUHK direct grant (No. 4442384). We also thank the beam time and technical supports provided by 19U2 beamline at SSRF, Shanghai. We appreciate Prof. Michael Toney for the openly accessible MATLAB tool box used for GIWAXS pattern indexing. N.Y. and F.Z. acknowledge funding from Knut and Alice Wallenberg Foundation under contract 2016.0059,

the Swedish Government Research Area in Materials Science on Functional Materials at Linköping University (Faculty Grant SFO-Mat-LiU No. 200900971) and China Scholarship Council (CSC) (No. 201708370115). The work at Arizona has been supported by the office of Naval Research, Award No. N00014-22-1-2178.

Author contributions

X.L. supervised the work. X.X. and L.M. contributed equally to this work. X.L. and X.X. conceived the idea. X.X. conducted the GIWAXS/GTSAXS measurements and crystal structure analysis. C.H., X.X. and R.S. conducted the device fabrication and characterization. L.M. performed all the theoretical calculations under the supervision of X.-K.C. Y.P. helped with DFT calculations. J.B. helped with the interpretation of the calculation results. Z.C. carried out the TAS measurement under supervision of H.Z. N.Y. conducted the FTPS-EQE and EQE_{EL} measurements under supervision of F.Z. M.Q. and Y.X. helped with the data analysis. Y.L. and Z.Z. provided the NFA material BTPR. X.X., L.M., X.-K.C and X.L. prepared the manuscript. All the authors discussed the results and commented on the manuscript.

Competing interests

The authors declare no competing interests.